Does Explicit Polarizability Improve Molecular-Dynamics Predictions of Glass Transition Temperatures of Ionic Liquids?

*Martin Klajmon and Ctirad Červinka**

Department of Physical Chemistry, Faculty of Chemical Engineering, University of Chemistry and Technology, Prague, Technická 5, 166 28 Prague 6, Czech Republic

*Corresponding author: cervinkc@vscht.cz

ABSTRACT

Molecular-dynamics simulations are used for predictions of the glass transition temperatures for a test set of 5 aprotic ionic liquids. Glass transitions are localized with the trend-shift method analyzing volumetric and transport properties of bulk amorphous phases. Classical non-polarizable all-atom OPLS force-field model developed by Canongia Lopes and Pádua (CL&P) is employed as the starting level of theory for all calculations. Alternative approaches of charge scaling and Drude oscillator model, accounting for atomic polarizability either implicitly or explicitly, respectively, are used to investigate the sensitivity of the glass transition temperatures to induction effects. The former non-polarizable model overestimates the glass transition temperature by tens of Kelvins (37 K in average). The charge scaling technique yields a significant improvement, and the best estimations were achieved using polarizable simulations with the Drude model, which yielded an average deviation of 11 K. Although the volumetric data usually exhibit a lesser trend shift upon vitrification, their lower statistical uncertainty enables to predict the glass transition temperature with a lower uncertainty than the ionic self-diffusivities, the temperature dependence of which is usually more scattered. Additional analyses of the simulated data were also performed, revealing that the Drude model predicts lower densities for most sub-cooled liquids, but higher densities for the glasses than the original CL&P, and that the Drude model also invokes some longer-range organization of the sub-cooled liquid, greatly impacting the temperature trend of ionic self-diffusivities in the low-temperature region.

1. INTRODUCTION

Knowledge of the melting temperature is a key prerequisite for each liquid material to become technologically applicable. However, numerous ionic liquids (ILs) have been reported not to crystallize upon cooling or to crystallize with difficulties and irreproducibility.[1] Large cohesive forces among the individual ions render the fluid highly viscous, which impedes the formation of a regular crystal lattice upon cooling. Instead, ILs often exhibit massive super-cooling of the liquid phase which undergoes a phase transition to an amorphous glass-like solid state at temperatures far below the equilibrium melting temperature. Knowledge of the respective glass transition temperature (T_g) thus becomes of utmost importance in the case of ILs.

All phase transitions are relatively slow processes, the time scale of which can hardly be sampled directly in all atom molecular-dynamics (MD) simulations covering at most dozens of nanoseconds for condensed-phase samples.[2] However, a phase transition is typically accompanied with a discontinuity in the temperature trend (or at least a trend shift) of the properties of the given material, such as its heat capacity, density, or diffusivity. Localization of the trend shift from simulated data then enables prediction of T_g between a solid amorphous glassy state and a liquid. Analyzing the temperature dependence of density or diffusivity enables thus in principle to derive the temperature of the phase transition between the liquid and glassy states.[3-5]

While experimental determinations of the heat capacity usually point to a possible phase transition, its high sensitivity to the computational noise makes it rather an unsuitable property to be observed computationally in this case. On the other hand, densities, which are closely related to molar volumes, have been reported to exhibit distinct trend shifts at the temperature of the glass transition for many macromolecular and low-molecular materials,[6-7] including ionic liquids.[1, 3, 8] Despite the principal simplicity of extraction of the densities from molecular simulations, concave temperature-dependence of densities of the amorphous phases of ionic liquids (IL) can be rather gradual throughout the phase

transition region, which complicates precise localization of T_g and leads to a larger statistical uncertainty of such determination of T_g. At the level of the non-polarizable force field, we illustrated that the computational uncertainty of T_g reaches 20 K for alkylimidazolium ILs,[1] but over 60 K for various pharmaceutic ingredients.[9]

Last but not least, the diffusivity of liquids and solids differs by several orders of magnitude by definition. Unfortunately, widespread non-polarizable force fields for IL tend to underestimate the diffusivities of IL by 1-2 orders of magnitude,[10-12] rendering the trend shift analysis of such miscalculated data rather problematic. This phenomenon clearly arises due to large electrostatic cohesive forces that arrange the ions into virtual cages that hinder other particles to move through.[13] Although there are also fixed-charge force fields[14-15] (usually using united atoms) that yield fairly accurate diffusivities with non-scaled atomic charges, a charge-scaling approach is nowadays commonly used to fix this issue of all-atom force fields, aiming to account for the missing polarizability of ions or charge transfer effects at least partially.[16-17] When all atomic charges are scaled by an empirical factor lesser than unity (around 0.8),[18] the resulting diffusivity of ILs matches experimental data appreciably better. Clearly, there are serious concerns about all the energetic aspects and credibility of the interaction energies and structural features resulting from this charge-scaling approach.[19-20]

An efficient way of modeling the atomic polarizability represents the Drude oscillator model.[21] It consists in replacing all polarizable atoms by two fictive particles connected by a harmonic oscillator bond – a heavy atomic core and a light electron cloud whose masses and charges summed together give the values of the original atom. In this way, the charge distribution of a molecule can fluctuate over time, which corresponds to formation of induced dipoles that respond to the outer electric field of surrounding ions. The Drude model has existed for some time, but its implementation in important MD codes, such as Lammps, was achieved only recently.[22] While there is an obvious computational way

how to parametrize the atomic polarizabilities from quantum chemical calculations,[23-24] optimum setup of the parameters of the fictive Drude electrons (mass, charge, force constant, damping of interactions of close Drude pairs) is still a subject of a scientific debate in the literature.[20, 25] These facts, together with an appreciably higher computational cost of polarizable MD in general, imped using polarizable simulations to study ILs-related phenomena, especially their phase transitions.

This work presents a detailed benchmark of MD-powered predictions of the glass transition temperatures of five synthetic aprotic ILs. The performance of the popular non-polarizable all-atom CL&P force field[26] and its polarizable CL&P-D successor[20] is compared. Moreover, within the non-polarizable CL&P FF, we also tested the approach with atomic charges scaled down by an empirical factor of 0.8. Thus, the total of three FF models were investigated for their performance in predicting T_g. The 5 ILs given, consisting of various archetypal cations and anions, were selected upon availability of the experimental data on T_g. The list of the considered ILs together with their chemical identifiers is provided in Table 1.

TABLE 1

Overview of the ILs included in this study and their chemical identifiers.

Ionic liquid	Formula	CAS RN
1-butyl-3-methylimidazolium bistriflimide	[bmIm][NTf_2]	174899-83-3
1-butyl-3-methylimidazolium triflate	[bmIm][OTf]	174899-66-2
1-butyl-3-methylimidazolium tosylate	[bmIm][OTs]	410522-18-8
1-butylpyridinium bistriflimide	[bPyri][NTf_2]	187863-42-9
1-butyl-1-methylpyrrolidinium bistriflimide	[bmPyrr][NTf_2]	223437-11-4

2. COMPUTATIONAL METHODS

2.1 MD Simulations

The three FF models applied to predict T_g are termed throughout this work as follows:

- **CL&P**: the original CL&P model (non-polarizable);
- **CL&P-scq**: the CL&P model with all atomic charges (q) scaled by a factor of 0.8 ($q^{\text{CL\&P-scq}} = 0.8\ q^{\text{CL\&P}}$) (non-polarizable);
- **CL&P-D$_k$**: CL&P combined with the Drude oscillator model (polarizable). (We use the term CL&P-D$_k$ in consistency with our recent paper,[25] although the term "CL&Pol" can also be found for this FF in the literature.[27])

To make the comparative study presented in this work as fair as possible, we used the same computational details regarding the MD simulations performed for all three FF models, at least where possible. The employed and thoroughly validated computational setup is based on our previous extensive computational studies addressing thermodynamic properties of IL using both non-polarizable[1, 28-29] and polarizable[25] models.

All MD simulations were performed in the LAMMPS package[22, 30-31] (version 29 Oct 2020). The initial configurations of the liquid-phase simulation boxes were generated by the PACKMOL program[32] and contained 300 to 480 IL pairs, depending on the number of atoms in the given IL pair. First, the simulation box from PACKMOL for each IL was pre-equilibrated for 10 ns at an elevated temperature of 400 K. Then, copies of the pre-equilibrated boxes were made and equilibrated for another 5 ns at different temperatures ranging from 100 to 400 K, followed by a production period of 10 ns at each temperature, sampling the system and recording the studied properties (mainly density and mean-square displacement) every 1000 fs. The velocity Verlet integrator with a time step value of 1 fs was used in all cases. The Nosé–Hoover (NH) thermostat and barostat were applied to control the

simulation temperature and pressure (always 0.1 MPa) in *NPT* ensembles, with update frequencies of 100 and 1000 fs, respectively. Regarding CL&P-D$_k$, we applied the temperature-grouped dual-NH thermostat developed by Son et al.[33] that improves equipartitioning of kinetic energy, which proved to be useful particularly for simulations with CL&P-D$_k$.[25]

For both the Coulombic and dispersion interactions, we set the cut-off distance to 12 Å. Long-range Coulombic interactions were computed using the particle–particle particle–mesh (PPPM) solver.

The original CL&P and CL&P-D$_k$ FF parameter values for the considered ions can be found in ref [34] and their original references in ref [25]. Atomic polarizability values, needed in the CL&P-D$_k$ model to calculate the charges of the Drude particles, were adopted from Schröder et al.[24] and corresponded to averaged values for individual atom types present in ILs.

The atomic Lennard–Jones pair potential parameters present in the original fixed-charge CL&P FF already implicitly account to some extent for the polarizability effects.[35] To avoid double-counting of those when CL&P is combined with the Drude model (CL&P-D$_k$), and to subtract the implicit polarization component from the attractive part of LJ, Pádua and his colleagues[20, 27, 35] proposed a methodology that determines scaling factors (k) for the energetic LJ parameters ε_{LJ} between different molecular fragments of ILs. This k-approach was considered in this work (hence the subscript k in CL&P-D$_k$) and the respective k values used to scale down the original ε_{LJ} parameters were taken from the literature.[20, 25] As a result, the atomic polarization was exclusively described by the Drude oscillators within the CL&P-D$_k$ model. The original LJ parameters σ_{LJ} from CL&P were kept unchanged.[25]

2.2 Evaluation of T_g

Two approaches were considered in this work to obtain glass transition temperatures from MD simulations: from the temperature-trend of (i) densities and (ii) diffusivities calculated using MD within the same trajectory. Both approaches are described in more detail below.

142 2.2.1 T_g from densities

143 Density (ρ) data simulated for each IL and each FF model in a temperature range of 100 to 400 K were
144 divided into two branches representing the glassy (approximately 100 to 200 K) and liquid
145 (approximately 250 to 400 K) phases. In some cases, the upper temperature bound of the glassy phase
146 and/or the lower bound of the liquid phase were modified in order to exclude outliers or data points
147 belonging to the vicinity of the T_g region, or to include more data points that still follow the linear
148 temperature-trend of the respective phase. A detailed overview of the data points used/excluded from
149 the linear regression and subsequent determination of T_g is shown in Figure S1. These branches of
150 simulated density points were linearly interpolated against the temperature. Subsequently, the
151 intersection of the obtained fitted lines determined the location of T_g, as illustrated in Figure S1. The
152 uncertainty of the simulated density data due to inefficient MD sampling was quantified using the
153 block-averaging technique.[36] However, the uncertainty of the linear regressions used to determine T_g
154 was found to be larger than the uncertainty estimated by the block-averaging technique. Therefore, the
155 final uncertainty in T_g^{ρ} was calculated based on the error propagation law from the uncertainties of the
156 linear regressions.[37]

157 2.2.2 T_g from diffusivities

158 The self-diffusivities (D) at each simulation temperature were determined from the simulated
159 equilibrium trajectories *via* the recommended Einstein relation:[38]

160 $$D = \frac{1}{6}\lim_{t\to\infty}\frac{\mathrm{d}}{\mathrm{d}t}\left\langle\left|\mathbf{r}(t)-\mathbf{r}(0)\right|^2\right\rangle, \qquad (1)$$

161 using the time-dependent mean-square displacement (MSD), that is, $\mathrm{MSD}(t) = \left\langle\left|\mathbf{r}(t)-\mathbf{r}(0)\right|^2\right\rangle$,
162 calculated from the molecular positions (**r**). The employed procedure to calculate T_g from D was similar
163 to that used in the case of densities: temperature dependent log(D) values, calculated from the slopes

of MSD *versus* time,[38] were divided into the glassy and liquid phases (roughly 100–200 K and 250–400 K, respectively). T_g was again evaluated from the intersection of the respective linear regressions. Again, the statistical uncertainty of the simulated data points turned out to be generally lower than that of the linear fit, so the final uncertainty in T_g^D was calculated from the latter. An overview of the data points used/excluded from the linear regression and the determined T_g values are shown in Figure S2. For each IL, the self-diffusivities and, hence, the corresponding T_g values were calculated separately for its cations, anions, and the ion pairs as a whole. However, no notable differences were observed among the T_g data determined from D of these three entities, as can be seen by comparing Figures S2, S3 and S4 in the Supporting Information. Therefore, we arbitrarily used those for cations, D_{cat}, to determine, assess, and discuss T_g^D estimates based on diffusivities in this work.

3. RESULTS AND DISCUSSION

Experimental glass transition temperatures and their counterparts calculated in this work (T_g^{ρ} and T_g^{D}) using the three different FF models for all five ILs are shown in Table 2 and displayed in Figure S5 and Figure S6, respectively, in the Supporting Information. Their determination from temperature-dependent data is summarized in Figures S1 and S2 in the Supporting Information; a sample of the T_g determination for [bmIm][NTf_2] is also shown in Figure 5. The deviations of the calculated T_g^{ρ} and T_g^{D} data from the experimental ones are shown in Figure 1 and Figure 3 below, respectively.

3.1 Glass transitions from densities

As can be seen in Table 2 and Figure 1, T_g^{ρ} values from CL&P are systematically overestimated by tens of Kelvins (up to ca. 65 K), with an absolute average deviation (AAD) of 37 K. This is in correspondence with our recent findings on T_g values for a series of [emIm]-based ILs.[1] Moreover, the T_g predictions from CL&P show the largest scatter in absolute deviations (16 K; see Table 2).

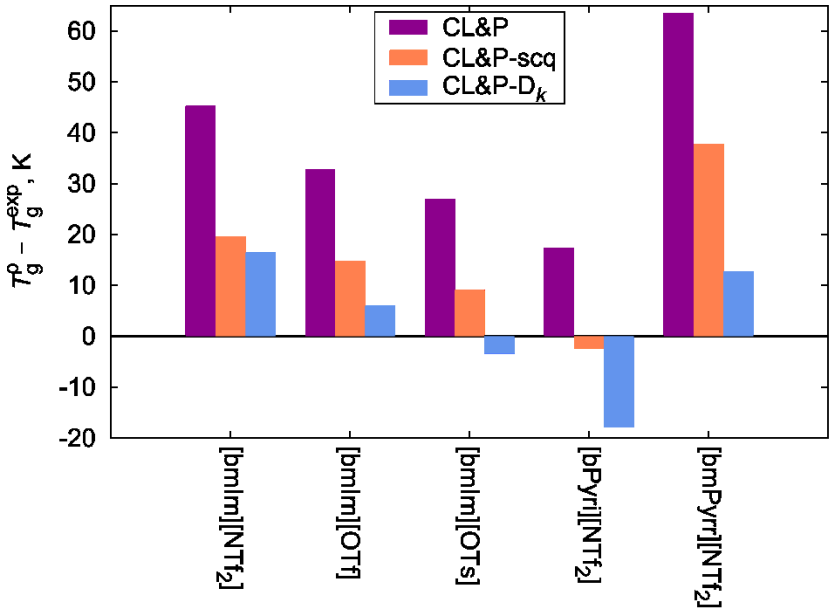

Figure 1. Deviations of T_g^{ρ} (calculated by MD from temperature-trend in densities) from experimental data for all 5 ILs.

CL&P-scq also tended to overestimate T_g values (for 4 out of 5 ILs), but the corresponding AAD was significantly lower (17 K), revealing a better quantitative performance of this scaled yet still non-polarizable variant of CL&P. Particularly notable is the quantitative performance of CL&P-scq for [bPyri][NTf_2] (deviation around −2 K).

Unlike the two non-polarizable models, CL&P-D$_k$ did not show a clear tendency to overpredict T_g, as an underestimation was found for 2 out of 5 ILs: [bmIm][OTs] and [bPyri][NTf_2]. AAD for CL&P-D$_k$ was 11 ± 6 K, making this FF the most accurate, robust and the least scattered approach for T_g^{ρ} predictions of ILs among the FFs tested in this work. Nearly quantitative predictions were obtained for [bmIm][OTf] and [bmIm][OTs], as can be seen in Figure 1.

T_g^{ρ} estimates from CL&P-scq compete with those from CL&P-D$_k$ in terms of quantitative accuracy (AADs 17 K and 11 K, respectively); moreover, CLP-scq simulations were significantly less computationally expensive (roughly 4 to 5-fold).

For each IL, T_g^{ρ} estimate from CL&P is always the highest one, followed by that from CL&P-scq, whereas T_g^{ρ} from CL&P-D$_k$ is always the lowest (that is, $T_g^{\text{CL\&P}} > T_g^{\text{CL\&P-scq}} > T_g^{\text{CL\&P-D}k}$). Moreover, the results of this work allow for evaluating the following average scaling factors between T_g values predicted by the different FF models:

$$T_g^{\text{CL\&P-scq}} = (0.91 \pm 0.01)\ T_g^{\text{CL\&P}};$$

$$T_g^{\text{CL\&P-D}k,} = (0.85 \pm 0.03)\ T_g^{\text{CL\&P}};$$

$$T_g^{\text{CL\&P-D}k} = (0.94 \pm 0.03)\ T_g^{\text{CL\&P-scq}}.$$

Therefore, for each individual IL, magnitude of the deviation between the predicted and experimental T_g^{ρ} data is largely determined by the exact location of the latter. For example, if CL&P largely overestimates T_g for an IL (as in the case of [bmIm][NTf_2]), CL&P-scq and CL&P-D$_k$ would probably decrease this error. On the other hand, if CL&P shows a relatively low error for an IL (as for

213 [bPyri][NTf_2]), a decrease in predicted T_g achieved by CL&P-scq and CL&P-D$_k$ may lead to a larger
214 (negative) error compared to CL&P, as really seen for CL&P-D$_k$ and [bPyri][NTf_2].
215 Fairly constant ratios between T_g values calculated with the different FF models are further reflected
216 in very similar slopes of the linear correlation between T_g^{ρ} and T_g^{exp}, as illustrated in Figure 2, although
217 the T_g predictions from the different FFs generally show different levels of correlation with their
218 experimental counterparts, as measured by the coefficient of determination (R^2 in Figure 2). Based on
219 the obtained R^2 values, CL&P-D$_k$ shows the best capability to rank the ILs according to their T_g
220 (R^2 = 0.40) among the tested FFs, followed by CL&P-scq and CL&P (R^2 = 0.35 and 0.18, respectively).
221 However, such R^2 values indicate a relatively weak correlation between the calculated and
222 experimental T_g data.
223 The IL [bmIm][OTs] shows the largest experimental T_g from the test set. All the three FF models
224 qualitatively correctly predicted this fact. However, CL&P and CL&P-scq did not qualitatively capture
225 the fact that [bmPyrr][NTf2] shows one of the lowest experimental T_g; they surprisingly predicted that
226 this IL has one of the largest T_g.

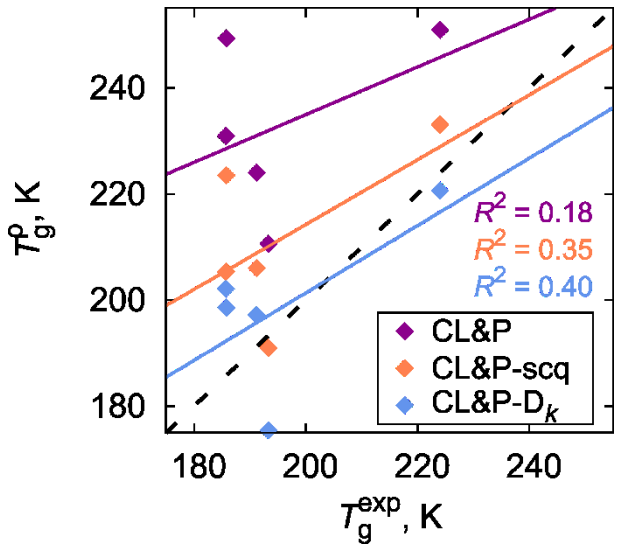

227
228 Figure 2. Diagonal comparison of experimental T_g and T_g^{ρ} calculated from temperature-trend in
229 densities.
230

TABLE 2

Comparison of Experimental Glass Transition Temperatures T_g (in K) with Their Counterparts Obtained from MD Simulations with Either Non-Polarizable (CL&P and CL&P-scq) or Polarizable (CL&P-D$_k$) Force Field Models.

Ionic liquid	T_g^{exp}	T_g^{MD} from ρ			T_g^{MD} from D_{cat}		
		CL&P	CL&P-scq	CL&P-D$_k$	CL&P	CL&P-scq	CL&P-D$_k$
[bmIm][NTf$_2$]	185.7[a]	231 ± 7	205 ± 7	202 ± 12	285 ± 17	255 ± 23	227 ± 22
[bmIm][OTf]	191.2[b]	224 ± 13	206 ± 14	197 ± 17	296 ± 34	262 ± 23	236 ± 17
[bmIm][OTs]	224.0[c]	251 ± 17	233 ± 8	221 ± 9	260 ± 24	247 ± 24	235 ± 27
[bPyri][NTf$_2$]	193.3[d]	211 ± 9	191 ± 7	175 ± 11	228 ± 22	215 ± 21	184 ± 20
[bmPyrr][NTf$_2$]	185.8[a]	249 ± 16	224 ± 7	199 ± 15	250 ± 22	240 ± 16	237 ± 32
AAD (K)[e]		37 ± 16	17 ± 12	11 ± 6	68 ± 30	48 ± 22	31 ± 18

[a] Averaged over the multiple experimental data available in the ILThermo database[39] (excluding obvious outliers).

[b] Ref [40]

[c] Ref [41]

[d] Ref [42]

[e] AAD is the average absolute deviation: $\mathrm{AAD} = N^{-1}\sum_{i=1}^{N}\left|T_{g,i}^{MD} - T_{g,i}^{exp}\right|$, where N denotes the number of ILs. The number after "±" represents standard deviation of the individual absolute deviations.

3.2 Analysis of the simulated densities

It can be seen in Figure S1 that the CL&P-scq model generally decreases the density of the glass and, in particular, the liquid phase compared to the original CL&P model, which seems intuitive as the charge-downscaling weakens the Coulombic forces between the cations and anions and under-binds the bulk phase. Regarding CL&P-D$_k$, although it also decreases densities of the liquid, densities on the glass branch are higher compared to those of both CL&P and CL&P-scq. This means that the glassy state simulated by CL&P-D$_k$ is denser, indicating stronger interactions predicted by CL&P-D$_k$ in this temperature region. This behavior is not seen for CL&P-scq, and a possible explanation could be that

the simple charge downscaling done in CL&P-scq is not compensated by any other effect, whereas in CL&P-D$_k$ the charge subtracted from an atom is not lost but assigned to the corresponding Drude particle.

Indeed, we demonstrate in Figure S7 that the electrostatic interactions among the permanent atomic charges are the most important contribution to the cohesion of bulk glassy phases at 150 K when the CL&P-D$_k$ model is applied. Absolute cohesion due to the electrostatics rises by 14% on average upon the transition from CL&P-D to CL&P-D$_k$. On the other hand, the dispersion contribution to the overall cohesion wanes appreciably (by 22%) when the CL&P-D$_k$ model is invoked. This seems counterintuitive, given that the CL&P-D$_k$ glasses are generally denser than those of CL&P. However, such a drop of the dispersion interactions in the polarizable glasses can be traced to downscaling the ε_{LJ} parameter of the LJ potential (see Section 2.1), leading to a decrease of magnitude of all dispersion interactions and/or to lowering the repulsion branch of the LJ potential curve. For the latter, stronger electrostatic interactions are, in some cases, capable of pushing non-bonded atoms, possessing the most significant partial charges, closer to one another, invoking even a weakly repulsing dispersion regime for the closest atomic contacts (but still with a negative interaction energy). This is demonstrated in Figure S8 in the Supporting Information using radial distribution functions (RDFs), $g(r)$, of C–O pair interactions for [bmIm][NTf$_2$] and [bmPyrr][NTf$_2$] (C represents selected carbon atoms of the cation ring, whereas O denotes the oxygen atoms of [NTf$_2$]; see Figure S8 for details). It can be seen that the peak maximum (3.19 Å) obtained from CL&P-D$_k$ at 150 K for the first coordination shell of [bmIm][NTf$_2$] is located at a mutual distance lower than the cross LJ parameter σ_{LJ}(C,O) = 3.25 Å, whereas that from CL&P (3.28 Å) is slightly higher than σ_{LJ}(C,O). This effect holds qualitatively even at an elevated temperature of 360 K. In the case of [bmPyrr][NTf$_2$], the C–O peak position (3.37 Å) from CL&P-D$_k$ at 150 K is slightly higher than the corresponding σ_{LJ}(C,O) value of 3.33 Å, but is still much closer to σ_{LJ}(C,O) than that from CL&P (3.54 Å), again indicating a more intensive packing of the CL&P-D$_k$ glass. Since the closest contact distances in bulk glassy [bmPyrr][NTf$_2$] simulated with

CL&P-D$_k$ still range in the attractive dispersion regime, shrinking of the glass due to turning-on the CL&P-D$_k$ model can be there more pronounced, unlike the case of [bmIm][NTf$_2$] where the already repulsive dispersion hinders further compression of the material.

Unfortunately, there are no experimental data for the sub-cooled liquid and glassy phases of the considered ILs in literature. To gain an insight about the possible accuracy of our simulations of bulk densities at low temperatures, we culled the experimental density data from the ILThermo database,[39] and extrapolated those high-temperature data down to 200 K (only to 220 K for [bmIm][OTs]) using the isobaric coefficient of thermal expansion, α_p, defined as:

$$\alpha_p = -\frac{1}{\rho}\left(\frac{\partial \rho}{\partial T}\right)_p . \qquad (2)$$

Note that for deriving the reference data, we accepted only those entries with reported uncertainties lower than 1 kg m^{-3} for [bmIm][NTf$_2$], [bmIm][OTf], and [bmPyrr][NTf$_2$]. Due to limited data availability, we loosened this threshold to 2 kg m^{-3} for [bmIm][OTs], and [bPyri][NTf$_2$]. The extrapolated experimental data could be considered as fairly reliable above 200 K (230 K for [bmIm][OTs]), being above the experimental T_g. All such selected experimental density data, along with the references to the original publications are summarized in Figures S9–S13.

Comparison of the calculated an experimental densities in Figures S9–S13 reveals that both CL&P and CL&P-D$_k$ models underestimate the bulk densities consistently at all temperatures for [bmIm][OTf], [bmIm][OTs], and [bPyri][NTf$_2$]. Both predicted density data sets are systematically overestimated for [bmIm][NTf$_2$], whereas the sign of the difference between theory and experiment depends on temperature and computational model for [bmPyrr][NTf$_2$]. In all cases except [bmPyrr][NTf$_2$], CL&P yields higher densities than the CL&P-D$_k$ model. The comparison of CL&P densities with extrapolated experimental data for liquid becomes misleading below 230 K as the simulations already predict the trend shift due to vitrification in that temperature region. In the low-temperature region (230– 270 K),

AARD of the calculated densities amounts to 2.7% and 3.2% for CL&P model and CL&P-D$_k$ models, respectively, whereas these AARD shift to 2.5% and 3.7% above 270 K on average.

3.3 Glass transitions from diffusivities

For T_g calculated from (cation) diffusivities, qualitative trends similar to those for T_g^{ρ} are seen. Namely, the following sequence can again be seen for the T_g results calculated from the different FFs for each IL: $T_g^{\text{CL\&P}} > T_g^{\text{CL\&P-scq}} > T_g^{\text{CL\&P-D}k}$. However, the average scaling factors between T_g data predicted by the different FF models are somewhat more scattered and differ more for individual ILs compared the obtained density-based T_g discussed in the previous section:

$$T_g^{\text{CL\&P-scq}} = (0.93 \pm 0.03) T_g^{\text{CL\&P}};$$

$$T_g^{\text{CL\&P-D}k,} = (0.85 \pm 0.06) T_g^{\text{CL\&P}};$$

$$T_g^{\text{CL\&P-D}k} = (0.92 \pm 0.05) T_g^{\text{CL\&P-scq}}.$$

Unlike for T_g^{ρ}, no correlation between experimental T_g and T_g^{D} is found, as shown in Figure 4 and indicated by the effectively zero R^2 values for all three FFs therein. This means that T_g estimates based on simulated diffusivities are inapplicable for ranking ILs even with CL&P-D$_k$, at least within the considered test set of ILs.

In terms of quantitative aspects, it can be seen in Table 2 and Figure 3 that T_g^{D} estimates generally show larger deviations from experimental data than those based on densities. AADs for CL&P, CL&P-scq and CL&P-D$_k$ now reach 68, 48 and 31 K, respectively, whereas it is only 37, 17 and 11 K for T_g^{ρ}. Note that the ILs [bmIm][NTf$_2$] and [bmIm][OTf] are the main contributors to these large AADs; for these ILs, CL&P overestimates T_g by approximately 100 K. The best predictions are again achieved from CL&P-D$_k$, followed by CL&P-scq and CL&P.

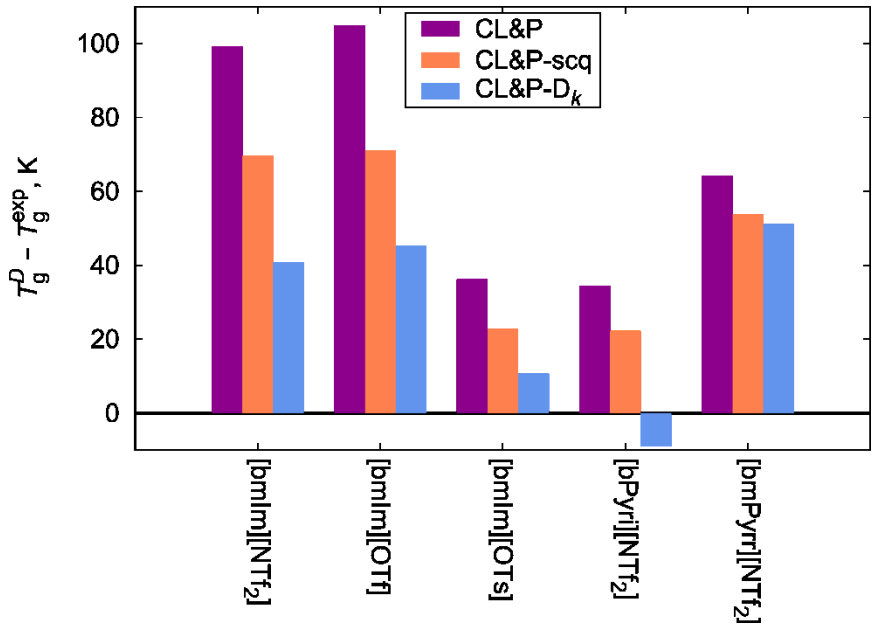

Figure 3. Deviations of T_g^D (calculated by MD from temperature-trend in cation diffusivities) from experimental data for all 5 ILs.

The uncertainties of the individual T_g^D values reported in Table 2 are also larger than their T_g^ρ counterparts. This is associated by the larger scatter of the simulated temperature-dependent diffusivity data compared to those on densities (compare Figures S1 and S2 in the Supporting Information), which can be attributed to the fact that the calculated diffusivities are not equilibrium averages over the simulated MD trajectory and are thus more challenging to compute accurately , especially in the context of obtaining a smooth temperature dependence.[38] On the other hand, the simulated diffusivities show a more significant temperature-trend shift upon melting of the glassy state in most cases compared to densities, as can be seen in Figures S1 and S2.

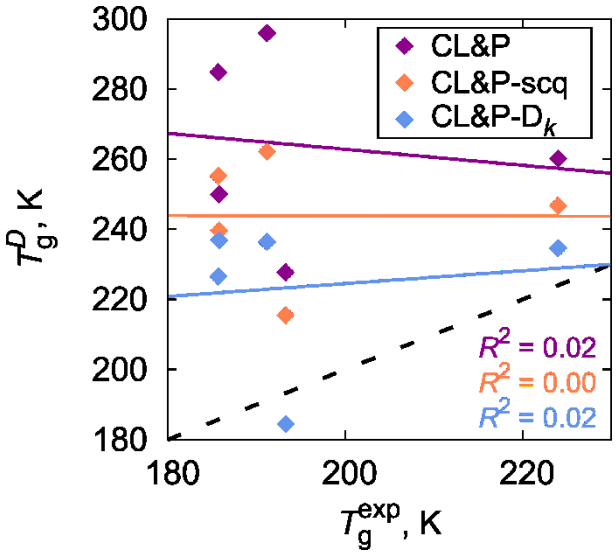

Figure 4. Diagonal comparison of experimental T_g and T_g^D calculated from temperature-trend in cation diffusivities.

3.4 Self-diffusivities of the sub-cooled liquid

Interestingly, temperature trends of the diffusivities computed from the non-polarizable and polarizable simulations differ qualitatively. A closer inspection of Figure S2 reveals that both the CL&P-D$_k$ and CL&P-scq models yield higher D values for the liquid at elevated temperatures, which justifies the motivation for introducing the polarizable simulations for ILs.[20] Upon cooling the liquid within CL&P-D$_k$, however, there is another well-observable trend shift of D in the region 250–350 K for all the considered liquids, attenuating the ionic self-diffusivity faster in CL&P-D$_k$ than it happens in CL&P. As a result, the self-diffusivities simulated for glasses using CL&P-D$_k$ are often lower than those resulting from the original CL&P model. In our test set, we observed this behavior for 3 out of 5 species, namely for [bmIm][NTf$_2$], [bmIm][OTf], and [bPyri][NTf$_2$].

This behavior of the simulated amorphous solids does not always correlate with the trends of predicted densities (a density increase of the glass in CL&P-D$_k$ does not necessarily lead to a drop of its self-diffusivity). To investigate this phenomenon further and to interpret it via any suitable structural aspects, we performed simulations of small-angle neutron diffraction for liquids and glasses at various

temperatures. Static structure factors for [bmIm][NTf_2] were calculated on the simulated trajectories (10 ns period for CL&P and 5 ns for CL&P-D$_k$) by the Diffraction utility,[43] using coherent scattering lengths for the elements from NIST,[44] the computational setup of which was previously validated for ILs.[45]

Figure 5 compares the structure factors (S) as functions of the reciprocal length (q) at various temperatures. All signals exhibit a broad peak around q=1.3–1.4 Å^{-1}, moving to smaller reciprocal lengths upon heating. This can be interpreted as an imprint of the closest atomic contacts (size of the first coordination shell is then 2π/1.4 Å^{-1} = 4.5 Å) in the bulk amorphous phases. Further, there is an undeniable shoulder peak below 0.9 Å^{-1} for the non-polarizable simulations of liquid, which can be attributed to a well-preserved cage structure of the second coordination shells (characteristic size is 2π/0.9 Å^{-1} = 7.0 Å) in ILs even at 400 K. This is usually interpreted as the principal artifact of non-polarizable simulations of ILs causing the massive underestimation of the predicted self-diffusivities of ions.[10, 12, 20] Note that there are no such analogous peaks for the liquid above 280 K in the CL&P-D$_k$ results.

In contrast, significant features of $S(q)$ appear in the temperature range 220–280 K (representing in fact sub-cooled liquid [bmIm][NTf_2]), for CL&P-D$_k$ trajectories. A sharp peak is manifested around 0.4 Å^{-1} at 250 K, becoming broader as the temperature increases. Furthermore, there is another well-pronounced peak above 0.2 Å^{-1}, being the most intense at 260 K. Such features of the structure factor indicate some form of longer-range ordering with characteristic size of 16 and 31 Å, respectively.

Note that these alterations of the structure factor appear in the exactly same temperature region, where the ionic self-diffusivities exhibit the steepest increase with temperature. A possible explanation could thus be that after melting of the glass using CL&P-D$_k$, the polarizable liquid phase organizes itself into distinct domains (spanning more than only two coordination shells), which restrain the ionic mobility at first, but the reorganization of which results in a steep increase of the mobility upon heating. Above 280 K, existence of such domains becomes improbable according to the CL&P-D$_k$ simulations, leading

to a shift of the diffusivity vs. temperature trend, and also to self-diffusivities already larger than in the non-polarizable model.

Trying to clarify the origin of these structural features, we calculated a series of RDFs for various different pairs of atoms within [bmIm][NTf_2] with CL&P-D$_k$ using an increased cut-off value of 30 Å to cover the long-range structural features of interest. Two different temperatures were considered: 250 K corresponding the mentioned sharp peak around 0.4 Å^{-1}, and an elevated temperature of 360 K, at which such structural features should be eliminated. However, the analysis shows no notable qualitative or quantitative differences between the RDFs calculated at both temperatures.

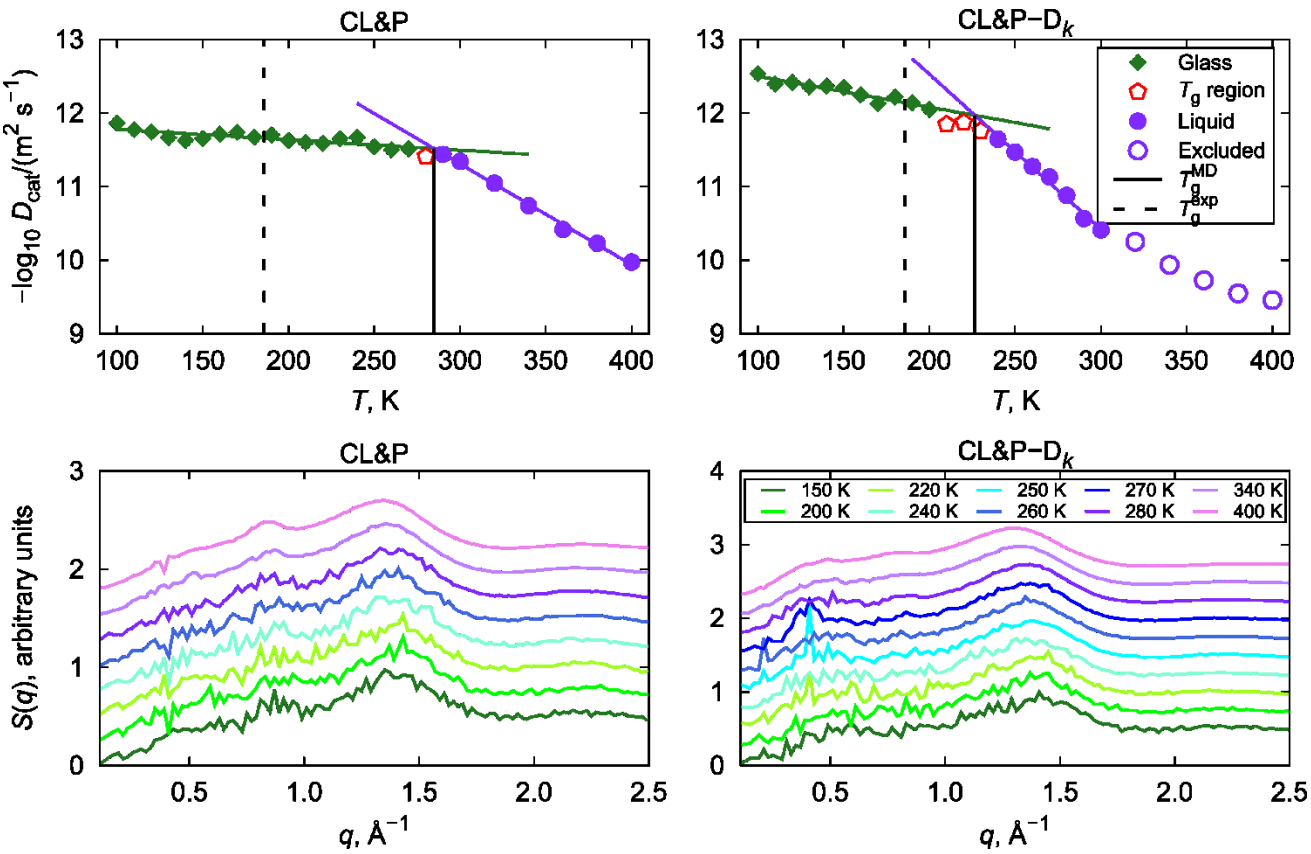

Figure 5. Determination of glass transition temperatures from simulated cation diffusivities (top) and structure factors, $S(q)$, calculated to mimic the small-angle neutron diffraction (bottom) considering the MD trajectories simulated for [bmIm][NTf_2] with the CL&P (left) and CL&P-D$_k$ (right) force fields. Note that the individual $S(q)$ curves are shifted artificially with respect to the corresponding temperature for a better readability of the plots.

4. CONCLUSIONS

The glass transition temperatures of five ILs obtained from MD simulations using three different FF models were evaluated and compared with the experimental counterparts. In all cases, the T_g values were determined using the temperature-trend shift method from both densities and cation diffusivities separately.

The CL&P-D$_k$ FF model shows the best general performance in predicting T_g, followed by the less sophisticated non-polarizable scaled-charge CL&P-scq and the original CL&P models. Determination of the glass transition temperature from the trend shift of the simulated densities is superior in terms of accuracy to that based on the diffusivities, although the densities typically show a less abrupt trend shift upon melting of the glassy state than the self-diffusivities do. It is the lesser scatter of the simulated temperature-dependent densities (compared to the diffusivities) that renders the density analysis more suitable for this purpose. The corresponding AAD values of the density-based predicted glass transition temperatures are 11, 17 and 37 K for CL&P-D$_k$, CL&P-scq and CL&P models, respectively. Such deviations still exceed the typical experimental uncertainties, which range within a few units of Kelvin. As a result, there is still space for a future search for a quantity that would exhibit an abrupt trend shift upon the glassy transition and that would be extractable from polarizable molecular simulations with a very low computational uncertainty to improve such predictions of the glass transition temperatures.

We also provide a few notes on some interesting observations regarding the simulated densities, diffusivities and their temperature trends, attempting to explain and interpret them at the molecular level. An indirect result of introducing the explicit polarizability (and scaling down the original dispersion interactions) is an appreciable increase of the densities of the sub-cooled liquids and glasses of ILs resulting from the CL&P-D$_k$ model. It appears that while the CL&P model tends to overstabilize the first and second solvation shells of the ions in the liquid, even at elevated temperatures, the CL&P-D$_k$ model predicts a longer-range ionic organization in the sub-cooled liquid, but just near-above the

glass transition temperature. Existence of these domains can significantly lower the ionic self-diffusivities for the highly sub-cooled liquids, as predicted with the CL&P-D_k model.

ASSOCIATED CONTENT

Supporting Information

The supporting information is available free of charge at DOI:

1. Illustration of the trend-shift method for analyzing the simulated densities and diffusivities.
2. Comparison of experimental and calculated glass transition temperatures by means of bar graphs.
3. Decomposition of the vaporization energy into individual mechanistic contributions.
4. Radial distribution functions of C–O for [bmIm][NTf_2] and [bmPyrr][NTf_2].
5. Comparison of experimental and calculated densities of liquids.

AUTHOR INFORMATION

Corresponding Author

* E-mail: cervinkc@vscht.cz

ACKNOWLEDGMENT

The authors acknowledge financial support from the Czech Science Foundation (GACR No. 19-04150Y). This work was supported by the Ministry of Education, Youth and Sports of the Czech Republic through the e-INFRA CZ (ID:90140).

435 REFERENCES

436 1. Červinka, C.; Štejfa, V., Computational Assessment of the Crystallization Tendency of 1-Ethyl-
437 3-methylimidazolium Ionic Liquids. *Physical Chemistry Chemical Physics* **2021,** *23*, 4951-4962.
438 2. Zhang, Y.; Maginn, E. J., A comparison of methods for melting point calculation using
439 molecular dynamics simulations. *J. Chem. Phys.* **2012,** *136* (14), 144116.
440 3. Habasaki, J.; Casalini, R.; Ngai, K. L., Molecular Dynamics Study of Thermodynamic Scaling
441 of the Glass-Transition Dynamics in Ionic Liquids over Wide Temperature and Pressure Ranges. *J.*
442 *Phys. Chem. B* **2010,** *114* (11), 3902-3911.
443 4. Habasaki, J.; Ngai, K. L., Molecular Dynamics Study of the Dynamics Near the Glass
444 Transition in Ionic Liquids. *Analyt. Sci.* **2008,** *24* (10), 1321-1327.
445 5. Zheng, L.; Luo, S.-N.; Thompson, D. L., Molecular dynamics simulations of melting and the
446 glass transition of nitromethane. *J. Chem. Phys.* **2006,** *124* (15), 154504.
447 6. Ghosh Dastidar, D.; Chakrabarti, G., Thermoresponsive Drug Delivery Systems,
448 Characterization and Application. In *Applications of Targeted Nano Drugs and Delivery Systems*,
449 Elsevier: 2019; pp 133-155.
450 7. Han, J.; Gee, R. H.; Boyd, R. H., Glass Transition Temperatures of Polymers from Molecular
451 Dynamics Simulations. *Macromolecules* **1994,** *27* (26), 7781-7784.
452 8. Rodríguez-Rivas, A.; Romero-Enrique, J. M.; Rull, L. F., Molecular simulation study of the
453 glass transition in a soft primitive model for ionic liquids. *Mol. Phys.* **2019**, 1-16.
454 9. Červinka, C.; Fulem, M., Structure and Glass Transition Temperature of Amorphous
455 Dispersions of Model Pharmaceuticals with Nucleobases from Molecular Dynamics. *Pharmaceutics*
456 **2021,** *13* (8).
457 10. Cadena, C.; Zhao, Q.; Snurr, R. Q.; Maginn, E. J., Molecular modeling and experimental studies
458 of the thermodynamic and transport properties of pyridinium-based ionic liquids. *J. Phys. Chem. B*
459 **2006,** *110* (6), 2821-2832.
460 11. Kirchner, B.; Holloczki, O.; Lopes, J. N. C.; Padua, A. A. H., Multiresolution calculation of
461 ionic liquids. *Wiley Interdiscip. Rev. Comput. Mol. Sci.* **2015,** *5* (2), 202-214.
462 12. Maginn, E. J., Atomistic simulation of the thermodynamic and transport properties of ionic
463 liquids. *Acc. Chem. Res.* **2007,** *40* (11), 1200-1207.
464 13. Canongia Lopes, J. N. A.; Padua, A. A. H., Nanostructural organization in ionic liquids. *J. Phys.*
465 *Chem. B* **2006,** *110* (7), 3330-3335.
466 14. Köddermann, T.; Reith, D.; Ludwig, R., Comparison of Force Fields on the Basis of Various
467 Model Approaches—How To Design the Best Model for the [CnMIM][NTf2] Family of Ionic Liquids.
468 *ChemPhysChem* **2013,** *14* (14), 3368-3374.
469 15. Son, C. Y.; McDaniel, J. G.; Schmidt, J. R.; Cui, Q.; Yethiraj, A., First-Principles United Atom
470 Force Field for the Ionic Liquid BMIM+BF4-: An Alternative to Charge Scaling. *J Phys Chem B* **2016,**
471 *120* (14), 3560-3568.
472 16. Zhang, Y.; Maginn, E. J., A Simple AIMD Approach to Derive Atomic Charges for Condensed
473 Phase Simulation of Ionic Liquids. *J. Phys. Chem. B* **2012,** *116* (33), 10036-10048.
474 17. Chaban, V., Polarizability versus mobility: atomistic force field for ionic liquids. *Physical*
475 *Chemistry Chemical Physics* **2011,** *13* (35), 16055-16062.
476 18. Vučemilović-Alagić, N.; Banhatti, R. D.; Stepić, R.; Wick, C. R.; Berger, D.; Gaimann, M. U.;
477 Baer, A.; Harting, J.; Smith, D. M.; Smith, A.-S., Insights from molecular dynamics simulations on
478 structural organization and diffusive dynamics of an ionic liquid at solid and vacuum interfaces. *J.*
479 *Colloid Interface Sci.* **2019,** *553*, 350-363.
480 19. Bedrov, D.; Piquemal, J.-P.; Borodin, O.; MacKerell, A. D.; Roux, B.; Schröder, C., Molecular
481 Dynamics Simulations of Ionic Liquids and Electrolytes Using Polarizable Force Fields. *Chem. Rev.*
482 **2019,** *119* (13), 7940-7995.

20. Goloviznina, K.; Canongia Lopes, J. N.; Costa Gomes, M.; Pádua, A. A. H., Transferable, Polarizable Force Field for Ionic Liquids. *J. Chem. Theory Comput.* **2019,** *15* (11), 5858-5871.
21. Guillaume, L.; Roux, B. t., Modeling induced polarization with classical Drude oscillators: Theory and molecular dynamics simulation algorithm. *J. Chem. Phys.* **2003,** *119* (6), 3025-3039.
22. Dequidt, A.; Devémy, J.; Pádua, A. A. H., Thermalized Drude Oscillators with the LAMMPS Molecular Dynamics Simulator. *J. Chem. Inf. Model.* **2016,** *56* (1), 260-268.
23. Bernardes, C. E. S.; Shimizu, K.; Lopes, J. N. C.; Marquetand, P.; Heid, E.; Steinhauser, O.; Schröder, C., Additive polarizabilities in ionic liquids. *Phys. Chem. Chem. Phys.* **2016,** *18* (3), 1665-1670.
24. Heid, E.; Szabadi, A.; Schröder, C., Quantum mechanical determination of atomic polarizabilities of ionic liquids. *Phys. Chem. Chem. Phys.* **2018,** *20* (16), 10992-10996.
25. Klajmon, M.; Červinka, C., Does Explicit Polarizability Improve Simulations of Phase Behavior of Ionic Liquids? *J. Chem. Theory Comput.* **2021,** *17* (10), 6225-6239.
26. Canongia Lopes, J. N.; Padua, A. A. H., CL&P: A generic and systematic force field for ionic liquids modeling. *Theor. Chem. Acc.* **2012,** *131* (3), 1129.
27. Goloviznina, K.; Gong, Z.; Padua, A. A. H., The CL&Pol polarizable force field for the simulation of ionic liquids and eutectic solvents. *Wires Comput Mol Sci* **2021**.
28. Červinka, C.; Pádua, A. A. H.; Fulem, M., Thermodynamic Properties of Selected Homologous Series of Ionic Liquids Calculated Using Molecular Dynamics. *J. Phys. Chem. B* **2016,** *120* (9), 2362-2371.
29. Červinka, C.; Klajmon, M.; Štejfa, V., Cohesive Properties of Ionic Liquids Calculated from First Principles. *Journal of Chemical Theory and Computation* **2019,** *15* (10), 5563-5578.
30. Plimpton, S.; Thompson, A.; Moore, S.; Kohlmayer, A., Large-scale Atomic/Molecular Massively Parallel Simulator. *Large-scale Atomic/Molecular Massively Parallel Simulator* **2018**.
31. Plimpton, S., Fast Parallel Algorithms for Short-Range Molecular Dynamics. *Journal of Computational Physics* **1995,** *117* (1), 1-19.
32. Martinez, L.; Andrade, R.; Birgin, E. G.; Martinez, J. M., PACKMOL: A Package for Building Initial Configurations for Molecular Dynamics Simulations. *J Comput Chem* **2009,** *30* (13), 2157-2164.
33. Son, C. Y.; McDaniel, J. G.; Cui, Q.; Yethiraj, A., Proper Thermal Equilibration of Simulations with Drude Polarizable Models: Temperature-Grouped Dual-Nose-Hoover Thermostat. *J Phys Chem Lett* **2019,** *10* (23), 7523-+.
34. Pádua, A. A. H.; Canongia Lopes, J. N. CL&P: Molecular force field for ionic liquids (il.ff). https://github.com/agiliopadua/ilff/blob/master/il.ff (accessed Nov 27, 2020).
35. Pádua, A. A. H., Resolving dispersion and induction components for polarisable molecular simulations of ionic liquids. *J. Chem. Phys.* **2017,** *146* (20), 204501.
36. Allen, M. P.; Tildesley, D. J., *Computer simulation of liquids*. Second edition. ed.; Oxford University Press: Oxford, United Kingdom, 2017; p xiv, 626 pages.
37. Navidi, W. C., *Statistics for engineers and scientists*. 3rd ed.; McGraw-Hill: New York, 2011; p xviii, 908 p.
38. Maginn, E. J.; Messerly, R. A.; Carlson, D. J.; Roe, D. R.; Elliot, J. R., Best Practices for Computing Transport Properties 1. Self-Diffusivity and Viscosity from Equilibrium Molecular Dynamics [Article v1.0]. *LiveCoMS* **2018,** *1* (1), 6324.
39. Dong, Q.; Muzny, C. D.; Kazakov, A.; Diky, V.; Magee, J. W.; Widegren, J. A.; Chirico, R. D.; Marsh, K. N.; Frenkel, M., ILThermo: A free-access web database for thermodynamic properties of ionic liquids. *J Chem Eng Data* **2007,** *52* (4), 1151-1159.
40. Tokuda, H.; Tsuzuki, S.; Susan, M. A. B. H.; Hayamizu, K.; Watanabe, M., How ionic are room-temperature ionic liquids? An indicator of the physicochemical properties. *J Phys Chem B* **2006,** *110* (39), 19593-19600.

41. Domanska, U.; Krolikowski, M., Phase equilibria study of the binary systems (1-butyl-3-methylimidazolium tosylate ionic liquid plus water, or organic solvent). *J Chem Thermodyn* **2010,** *42* (3), 355-362.
42. Kocian, Š.; Štejfa, V., Personal communication.
43. Dequidt, A. *Diffraction code*, Université Clermont Auvergne, 2016.
44. Research, N. C. f. N. Neutron Scattering Lengths and Cross Sections of the Elements and Their Isotopes. https://www.ncnr.nist.gov/resources/n-lengths/list.html (accessed Dec 15, 2021).
45. Mao, X.; Brown, P.; Červinka, C.; Hazell, G.; Li, H.; Ren, Y.; Chen, D.; Atkin, R.; Eastoe, J.; Grillo, I.; Padua, A. A. H.; Costa Gomes, M. F.; Hatton, T. A., Self-assembled nanostructures in ionic liquids facilitate charge storage at electrified interfaces. *Nature Mater.* **2019,** *18* (12), 1350-1357.

543 Table of contents

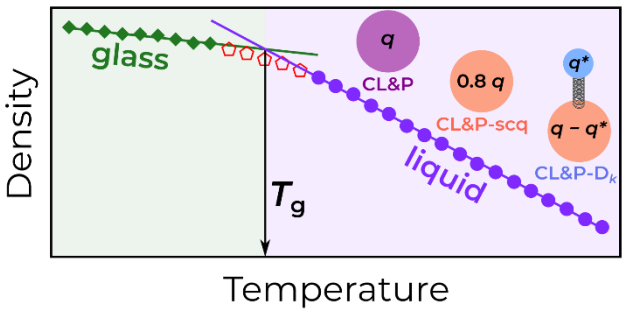

544

545

546

Supporting Information

Does Explicit Polarizability Improve Molecular-Dynamics Predictions of Glass Transition Temperatures of Ionic Liquids?

Martin Klajmon and Ctirad Červinka*

Department of Physical Chemistry, Faculty of Chemical Engineering, University of Chemistry and Technology, Prague, Technická 5, 166 28 Prague 6, Czech Republic

**Corresponding author: cervinkc@vscht.cz*

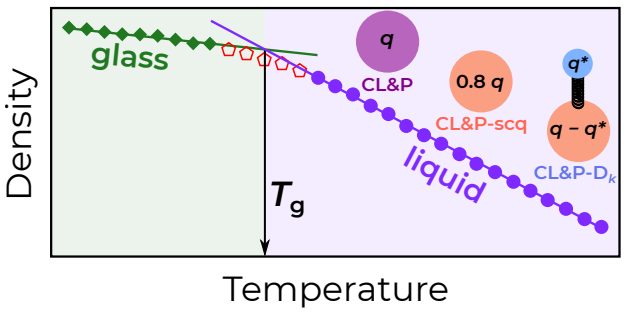

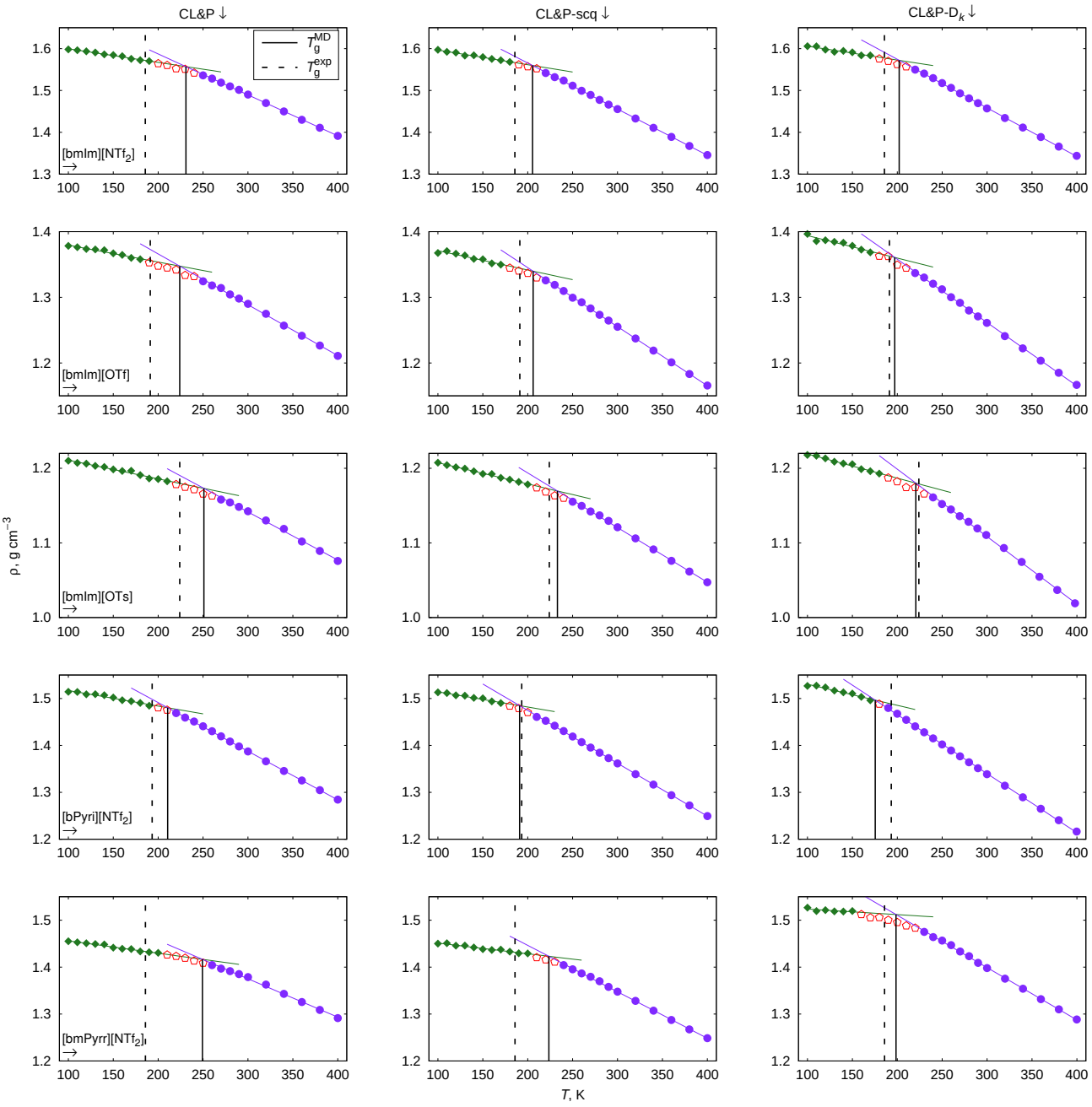

Figure S1: Determination of the glass transition temperatures (T_g) of the considered ionic liquids by the trend shift method from the temperature-dependent densities simulated by the three different force field models. Green and purple points were used for linear extrapolations of the trends of the glassy and liquid phases, respectively. Data points excluded from the T_g evaluation are displayed with empty points.

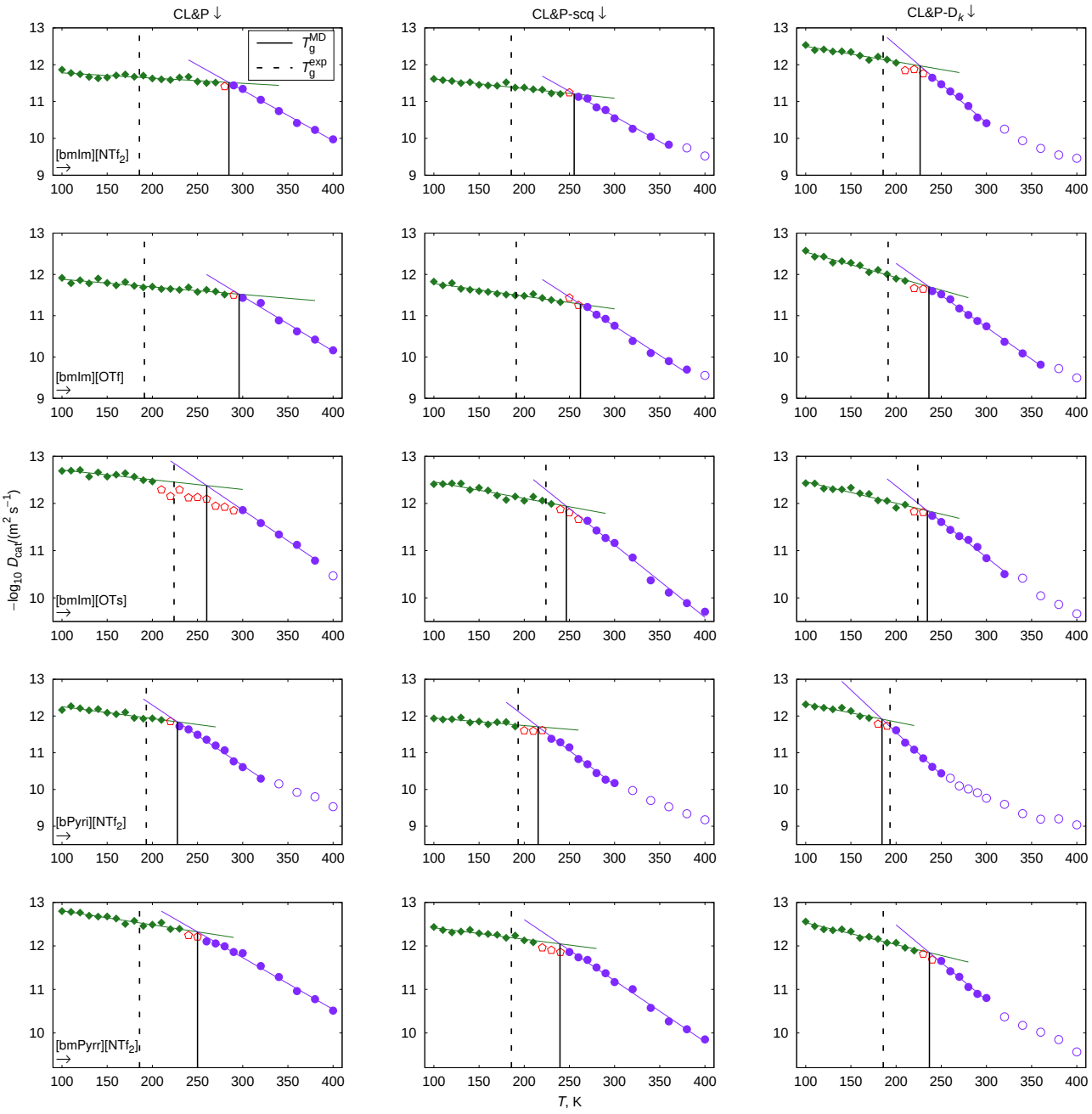

Figure S2: Determination of the glass transition temperatures (T_g) of the considered ionic liquids by the trend shift method from the temperature-dependent **cation** diffusivities simulated by the three different force field models. Green and purple points were used for linear extrapolations of the trends of the glassy and liquid phases, respectively. Data points excluded from the T_g evaluation are displayed with empty points.

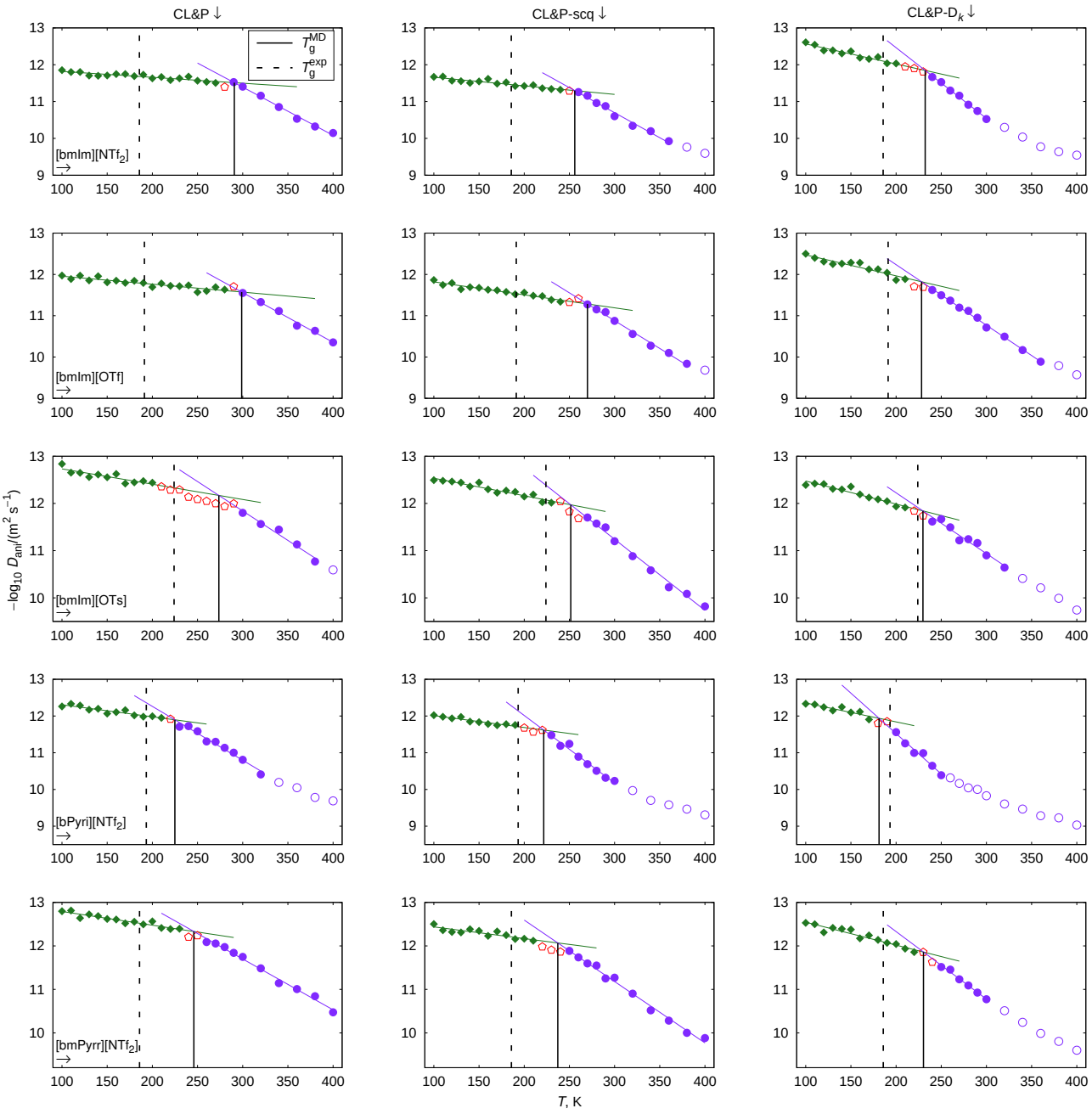

Figure S3: Determination of the glass transition temperatures (T_g) of the considered ionic liquids by the trend shift method from the temperature-dependent **anion** diffusivities. The symbols have the same meaning as in Figure S2.

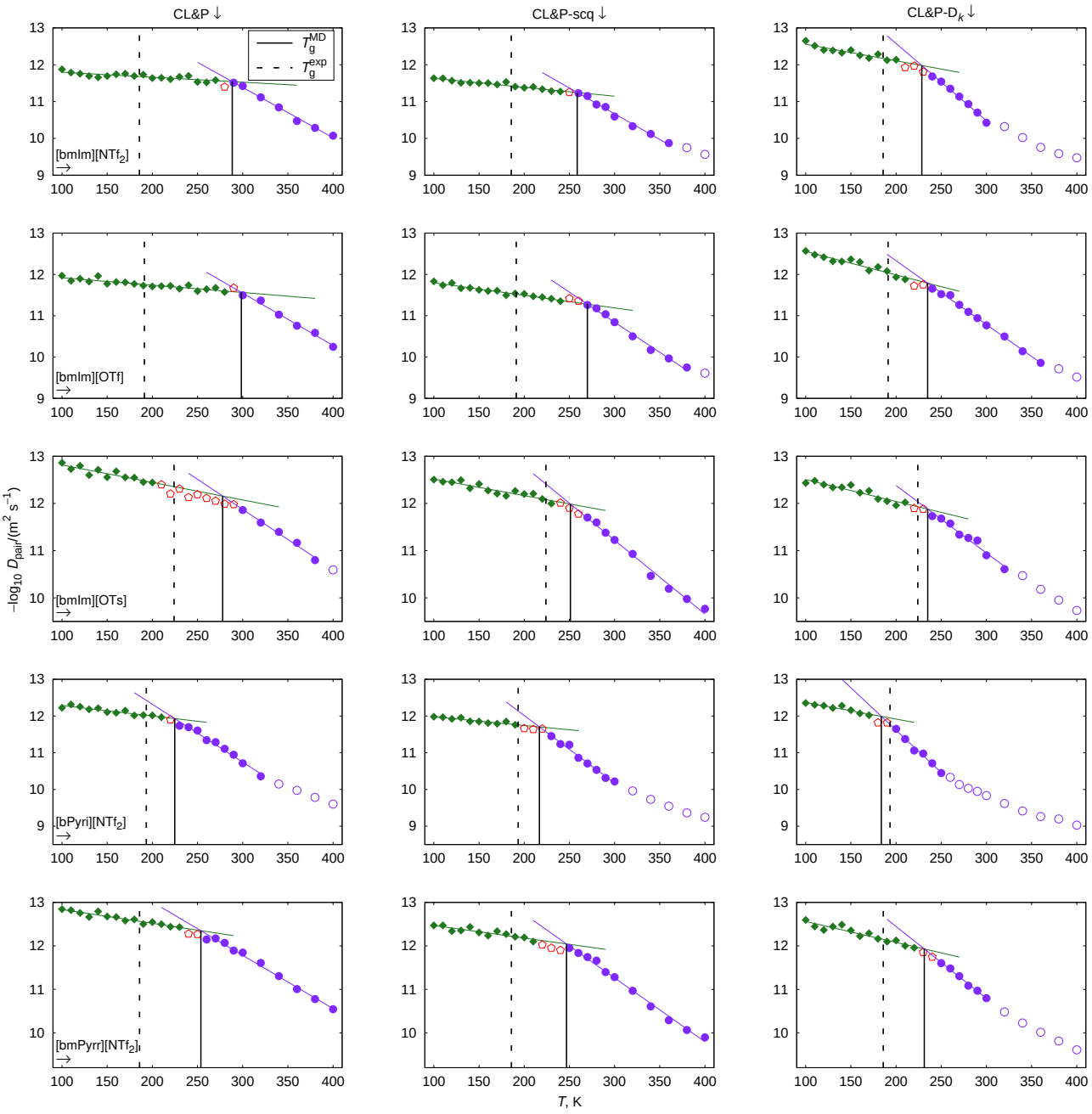

Figure S4: Determination of the glass transition temperatures (T_g) of the considered ionic liquids by the trend shift method from the temperature-dependent **ion-pair** diffusivities. The symbols have the same meaning as in Figure S2.

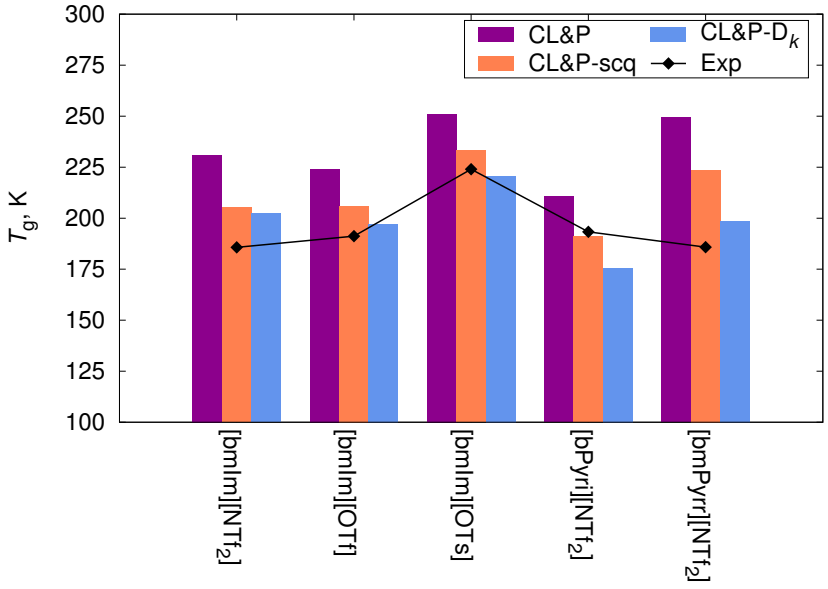

Figure S5: Comparison of experimental T_g values and those calculated in this work from densities (T_g^{ρ}) simulated using the various force field models for all 5 ILs.

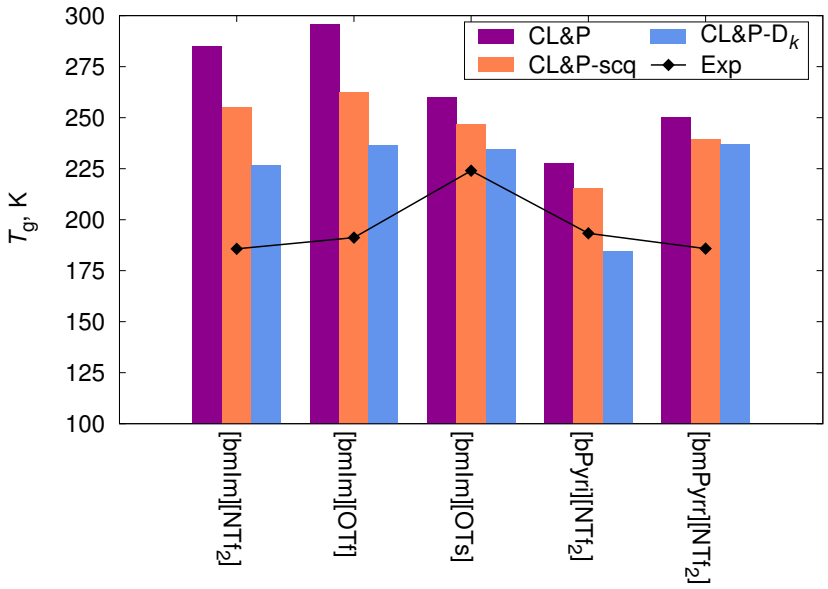

Figure S6: Comparison of experimental T_g values and those calculated in this work from cation diffusivities (T_g^{D}) simulated using the various force field models for all 5 ILs.

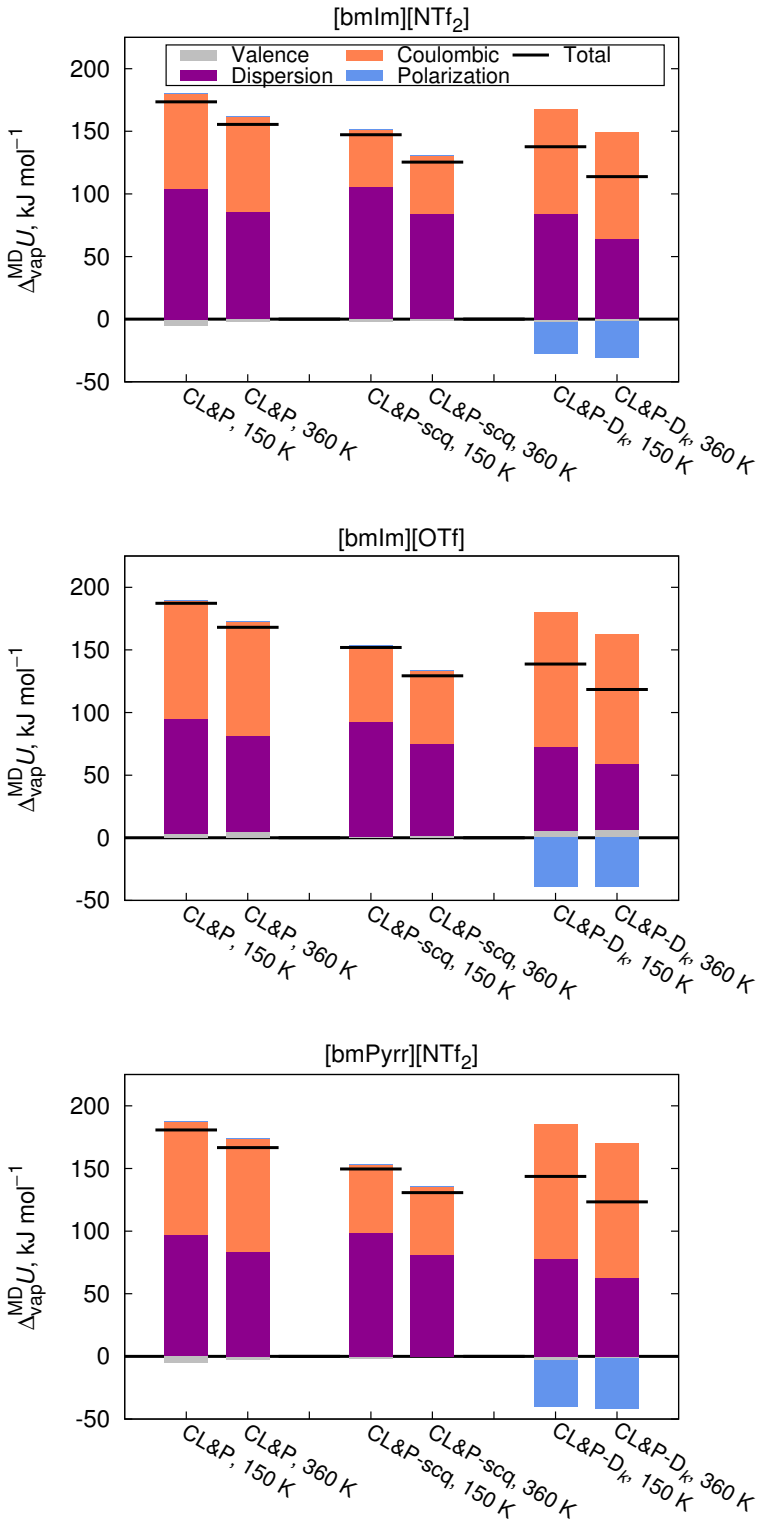

Figure S7: Vaporization energies and their individual mechanistic components calculated for [bmIm][NTf_2], [bmIm][OTf], and [bmPyrr][NTf_2] using the various force field models.

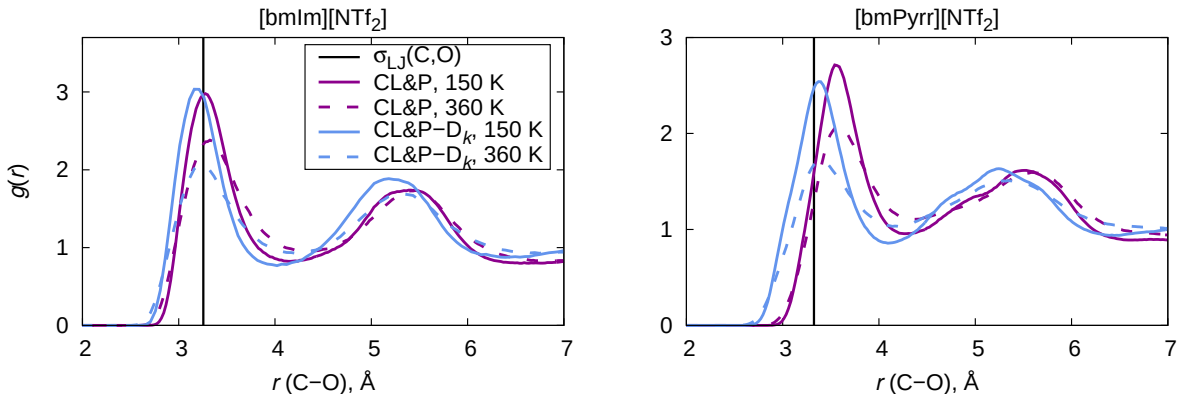

Figure S8: Radial distribution functions of C–O calculated for [bmIm][NTf_2] and [bmPyrr][NTf_2] using the CL&P and CL&P-D_k force field models at two different temperatures. For [bmIm], C represents the C_2 atom of the imidazolium ring, whereas it corresponds to the C_2 and C_5 atoms of the pyrrolidinium ring in [bmPyrr]. O represents the oxygen atoms of [NTf_2].

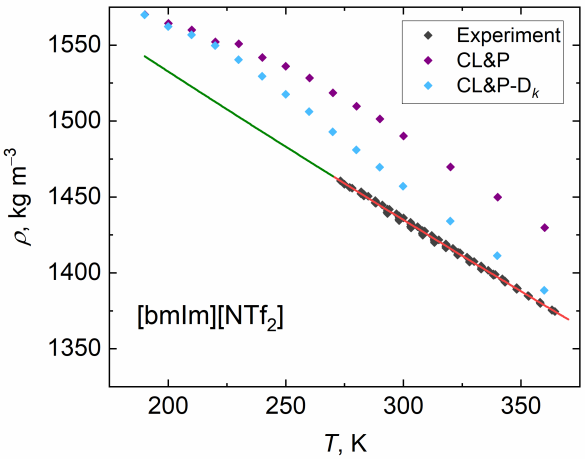

Figure S9: Comparison of calculated and experimental [1–9] densities of liquid [bmIm][NTf_2].

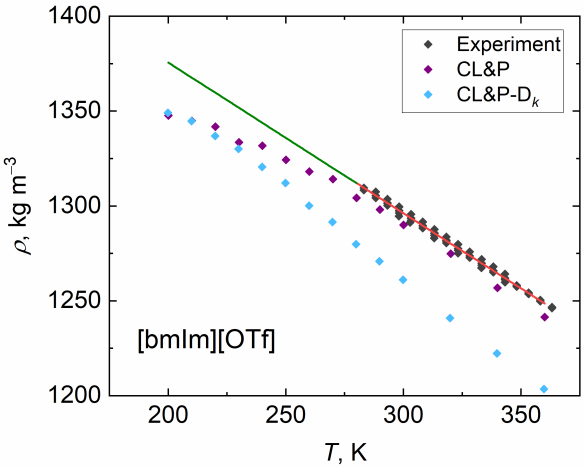

Figure S10: Comparison of calculated and experimental [10–15] densities of liquid [bmIm][OTf].

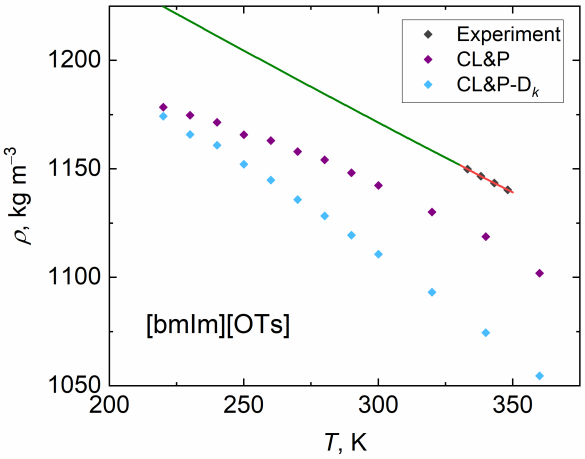

Figure S11: Comparison of calculated and experimental [16] densities of liquid [bmIm][OTs].

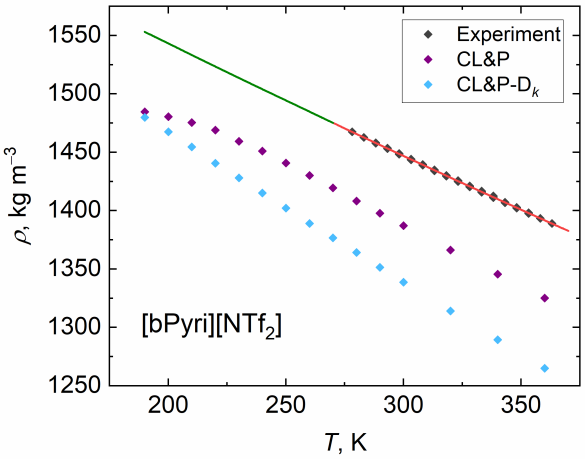

Figure S12: Comparison of calculated and experimental [17–21] densities of liquid [bPyri][NTf_2].

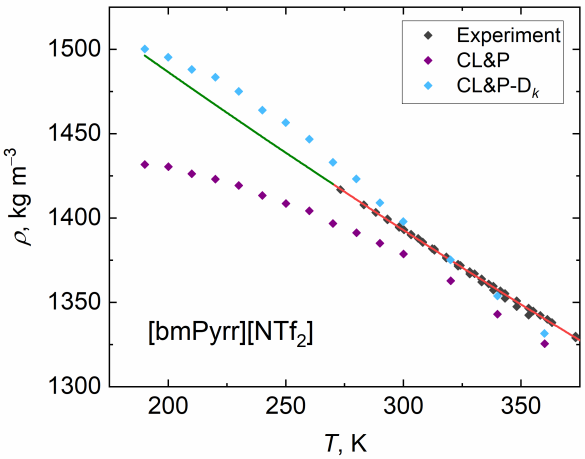

Figure S13: Comparison of calculated and experimental [10, 11, 22–27] densities of liquid [bmPyrr][NTf_2].

References

[1] Almeida, H. F. D.; Canongia Lopes, J. N.; Rebelo, L. P. N.; Coutinho, J. A. P.; Freire, M. G.; Marrucho, I. M. Densities and Viscosities of Mixtures of Two Ionic Liquids Containing a Common Cation. **2016**, *61*, 2828–2843.

[2] Zorębski, M.; Zorębski, E.; Dzida, M.; Skowronek, J.; Jężak, S.; Goodrich, P.; Jacquemin, J. Ultrasonic Relaxation Study of 1-Alkyl-3-methylimidazolium-Based Room-Temperature Ionic Liquids: Probing the Role of Alkyl Chain Length in the Cation. **2016**, *120*, 3569–3581.

[3] Widowati, E.; Lee, M.-J. P–V–T properties of binary mixtures of the ionic liquid 1-butyl-3-methylimidazolium bis(trifluoromethylsulfonyl)imide with anisole or acetophenone at elevated pressures. **2013**, *63*, 95–101.

[4] Součková, M.; Klomfar, J.; Pátek, J. Measurements and group contribution analysis of 0.1MPa densities for still poorly studied ionic liquids with the [PF6] and [NTf2] anions. **2014**, *77*, 31–39.

[5] Khalil, R.; Chaabene, N.; Azar, M.; Malham, I. B.; Turmine, M. Effect of the chain lengthening on transport properties of imidazolium-based ionic liquids. **2020**, *503*, 112316.

[6] Kanakubo, M.; Harris, K. R. Density of 1-Butyl-3-methylimidazolium Bis(trifluoromethanesulfonyl)amide and 1-Hexyl-3-methylimidazolium Bis(trifluoromethanesulfonyl)amide over an Extended Pressure Range up to 250 MPa. **2015**, *60*, 1408–1418.

[7] Jacquemin, J.; Husson, P.; Majer, V.; Costa Gomes, M. F. Influence of the Cation on the Solubility of CO2 and H2 in Ionic Liquids Based on the Bis(trifluoromethylsulfonyl)imide Anion. **2007**, *36*, 967–979.

[8] Gomes de Azevedo, R.; Esperança, J. M. S. S.; Szydlowski, J.; Visak, Z. P.; Pires, P. F.; Guedes, H. J. R.; Rebelo, L. P. N. Thermophysical and thermodynamic properties of ionic liquids over an extended pressure range: [bmim][NTf2] and [hmim][NTf2]. **2005**, *37*, 888–899.

[9] Geppert-Rybczyńska, M.; Sitarek, M. Acoustic and Volumetric Properties of Binary Mixtures of Ionic Liquid 1-Butyl-3-methylimidazolium Bis(trifluoromethylsulfonyl)imide with Acetonitrile and Tetrahydrofuran. **2014**, *59*, 1213–1224.

[10] Seoane, R. G.; Corderí, S.; Gómez, E.; Calvar, N.; González, E. J.; Macedo, E. A.; Domínguez, n. Temperature Dependence and Structural Influence on the Thermophysical Properties of Eleven Commercial Ionic Liquids. **2012**, *51*, 2492–2504.

[11] Musiał, M.; Zorębski, E.; Zorębski, M.; Dzida, M. Effect of alkyl chain length in cation on thermophysical properties of two homologous series: 1-alkyl-1-methylpyrrolidinium bis(trifluoromethylsulfonyl)imides and 1-alkyl-3-methylimidazolium trifluoromethanesulfonates. **2019**, *293*, 111511.

[12] Mbondo Tsamba, B. E.; Sarraute, S.; Traïkia, M.; Husson, P. Transport Properties and Ionic Association in Pure Imidazolium-Based Ionic Liquids as a Function of Temperature. **2014**, *59*, 1747–1754.

[13] González, E. J.; Domínguez, n.; Macedo, E. A. Physical and Excess Properties of Eight Binary Mixtures Containing Water and Ionic Liquids. **2012**, *57*, 2165–2176.

[14] González, E. J.; Calvar, N.; Domínguez, n.; Macedo, E. A. Osmotic and apparent molar properties of binary mixtures alcohol+1-butyl-3-methylimidazolium trifluoromethanesulfonate ionic liquid. **2013**, *61*, 64–73.

[15] García-Miaja, G.; Troncoso, J.; Romaní, L. Excess properties for binary systems ionic liquid+ethanol: Experimental results and theoretical description using the ERAS model. **2008**, *274*, 59–67.

[16] Domańska, U.; Królikowski, M. Phase equilibria study of the binary systems (1-butyl-3-methylimidazolium tosylate ionic liquid+water, or organic solvent). **2010**, *42*, 355–362.

[17] Zeng, S.; Wang, J.; Bai, L.; Wang, B.; Gao, H.; Shang, D.; Zhang, X.; Zhang, S. Highly Selective Capture of CO2 by Ether-Functionalized Pyridinium Ionic Liquids with Low Viscosity. **2015**, *29*, 6039–6048.

[18] Santos, D.; Santos, M.; Franceschi, E.; Dariva, C.; Barison, A.; Mattedi, S. Experimental Density of Ionic Liquids and Thermodynamic Modeling with Group Contribution Equation of State Based on the Lattice Fluid Theory. **2016**, *61*, 348–353.

[19] Oliveira, F. S.; Freire, M. G.; Carvalho, P. J.; Coutinho, J. A. P.; Lopes, J. N. C.; Rebelo, L. P. N.; Marrucho, I. M. Structural and Positional Isomerism Influence in the Physical Properties of Pyridinium NTf2-Based Ionic Liquids: Pure and Water-Saturated Mixtures. **2010**, *55*, 4514–4520.

[20] Larriba, M.; García, S.; Navarro, P.; García, J.; Rodríguez, F. Physical Properties of N-Butylpyridinium Tetrafluoroborate and N-Butylpyridinium Bis(trifluoromethylsulfonyl)imide Binary Ionic Liquid Mixtures. **2012**, *57*, 1318–1325.

[21] Bounsiar, R.; Gascón, I.; Amireche, F.; Lafuente, C. Volumetric properties of three pyridinium-based ionic liquids with a common cation or anion. **2020**, *521*, 112732.

[22] Geppert-Rybczyńska, M.; Lehmann, J. K.; Heintz, A. Physicochemical properties of two 1-alkyl-1-methylpyrrolidinium bis[(trifluoromethyl)sulfonyl]imide ionic liquids and of binary mixtures of 1-butyl-1-methylpyrrolidinium bis[(trifluoromethyl)sulfonyl]imide with methanol or acetonitrile. **2014**, *71*, 171–181.

[23] Harris, K. R.; Woolf, L. A.; Kanakubo, M.; Rüther, T. Transport Properties of N-Butyl-N-methylpyrrolidinium Bis(trifluoromethylsulfonyl)amide. **2011**, *56*, 4672–4685.

[24] Sánchez-Ramírez, N.; Assresahegn, B. D.; Bélanger, D.; Torresi, R. M. A Comparison among Viscosity, Density, Conductivity, and Electrochemical Windows of N-n-Butyl-N-methylpyrrolidinium and Triethyl-n-pentylphosphonium Bis(fluorosulfonyl imide) Ionic Liquids and Their Analogues Containing Bis(trifluoromethylsulfonyl) Imide Anion. **2017**, *62*, 3437–3444.

[25] Sas, O. G.; Ivaniš, G. R.; Kijevčanin, M. L.; González, B.; Domínguez, A.; Radović, I. R. Densities and Derived Volumetric Properties of Ionic Liquids with [Nf2] and [NTf2] Anions at High Pressures. **2018**, *63*, 954–964.

[26] Vraneš, M.; Dožić, S.; Djeric, V.; Gadžurić, S. Physicochemical Characterization of 1-Butyl-3-methylimidazolium and 1-Butyl-1-methylpyrrolidinium Bis(trifluoromethylsulfonyl)imide. **2012**, *57*, 1072–1077.

[27] Vraneš, M.; Tot, A.; Papović, S.; Zec, N.; Dožić, S.; Gadžurić, S. Ideal and non-ideal behaviour of 1-butyl-1-methylpyrrolydinium bis(trifluoromethylsulfonyl)imide+γ-butyrolactone binary mixtures. **2015**, *81*, 66–76.